# Numerical investigation of the flow properties of He II

R. G. K. M. Aarts and A. T. A. M. de Waele
*Physics Department, Eindhoven University of Technology, P.O. Box 513, NL-5600 MB Eindhoven, The Netherlands*
(Received 17 March 1994)

In the framework of the reconnecting vortex-tangle model, flow properties of He II were studied numerically. The Crank-Nicolson method was used to calculate the motion of quantized $^4$He vortices, assuming smooth walls in infinitely long channels, applying periodic boundary conditions in the direction of the flow, and with friction coefficients $\alpha=0.1$ and $\alpha'=0$. Flow channels with square and circular cross sections and infinitely wide slits were studied. The superfluid velocity profile was assumed to be flat; the normal-component velocity profile was either flat or parabolic. Special interest was paid to the time-averaged line-length density and the average mutual-friction force density as functions of the difference between the average normal-fluid velocity and the externally applied superfluid velocity. The influence of the periodicity length on the calculated flow properties was determined. The results were compared with experiment.

## I. INTRODUCTION

The flow properties of superfluid helium show a rich variety of phenomena.[1,2] The mutual friction between the superfluid and the normal components, which is observed above well-defined critical velocities, is attributed to the presence of quantized vortices in the superfluid. Numerical simulation of the motion of these vortices is a powerful tool for the theoretical investigation of the flow properties of $^4$He II and $^3$He-$^4$He II mixtures.[3–7] In this paper we concentrate on the numerical study of flow properties of He II in infinitely long channels with smooth walls. The channel cross sections were square, circular, and (infinitely wide) slits (Fig. 1). Periodic boundary conditions were applied in the flow direction (the $z$ direction). The influence of the magnitude of the periodicity length $l$ was investigated. The externally applied superfluid velocity was assumed to be constant (flat velocity profile); the profile of the normal component was either flat (plug flow) or parabolic (Poiseuille flow).

## II. THE NUMERICAL APPROACH

### A. Velocity fields

The velocity of the superfluid component $\mathbf{v}_s$ can be written as the sum of three contributions

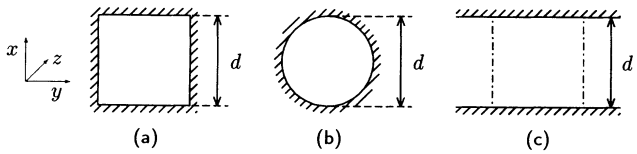


FIG. 1. Cross sections of channels studied in this work. The $z$ axis is the flow direction, the cross sections are in the $xy$ plane. We distinguish (a) a square cross section, (b) circular channels, and (c) a slit extending infinitely in the $y$ direction. At the dotted lines periodic boundary conditions were applied.

$$\mathbf{v}_s = V_s + \mathbf{v}_i + \mathbf{v}_b \tag{1}$$

in which $V_s$ represents the externally applied superflow, which for our channels is homogeneous, and $\mathbf{v}_i$ the velocity induced by the vortices. The contribution $\mathbf{v}_b$ is due to the boundary condition $\mathbf{v}_{s\perp}=0$, which, in the case of a flat wall, can be regarded as due to mirror vortices.

On length scales much larger than the diameter $a_0=0.1$ nm of the vortex core a vortex can be approximated by a line in space represented by the relation

$$\mathbf{s}=\mathbf{s}(\xi)\ , \tag{2}$$

where $\xi$ is a parameter defining a point $s$ on the vortex line. In this paper we take $\xi$ as the length of the part of the vortex line between the point in question and some suitably chosen reference point on the line. The velocity of a point on the line is given by

$$\frac{d\mathbf{s}}{dt}=\mathbf{v}_s+\alpha\mathbf{s}'\times(\mathbf{v}_n-\mathbf{v}_s)-\alpha'(\mathbf{v}_n-\mathbf{v}_s) \tag{3}$$

in which $\mathbf{v}_n$ is the velocity of the normal component, and $\alpha$ and $\alpha'$ are the friction parameters.[8] In this paper we will neglect the $\alpha'$ term, and we limit our calculations to the isothermal case of $\alpha=0.1$, which in pure $^4$He, corresponds to a temperature of 1.6 K.

The velocity $\mathbf{v}_i$, induced by the vortex lines, can be calculated from the Biot-Savart expression

$$\mathbf{v}_i(\mathbf{s})=\frac{\kappa}{4\pi}\int_\delta \frac{(\mathbf{r}-\mathbf{s})\times d\mathbf{r}}{|\mathbf{r}-\mathbf{s}|^3}\ , \tag{4}$$

where $\kappa=1.0\times10^{-7}$ m/s$^2$ is the vortex strength. The index $\delta$ indicates that the integral is taken along the entire vortex line except for a region of length $\delta$ on both sides of the point $s$. The value of $\delta$ is chosen in such a way that the calculated velocity of a vortex ring satisfies experiment; we took $\delta=0.64a_0$.

In capillaries with square cross sections only flat normal-fluid velocity profiles were considered (plug flow). In circular capillaries the velocity profiles of the normal

 

component were assumed to be parabolic (Poiseuille flow)

$$\mathbf{v}_n = 2V_n \left[1 - \frac{4r^2}{d^2}\right] \mathbf{e}_z \ . \tag{5}$$

Here $r$ is the radius, $d$ the tube diameter, and $V_n$ is the normal fluid velocity averaged over the tube cross section

$$V_n = \overline{v_n} \ . \tag{6}$$

In slits both parabolic and flat normal velocity profiles were studied. Due to the assumption of perfectly smooth walls, the case with nonzero superflow and zero normal velocity is equivalent with the case of a normal-fluid plug flow and zero superfluid velocity. These two cases will be treated equivalently.

We introduce the difference of $\mathbf{v}_n$ and the *applied* superfluid velocity $\mathbf{V}_s$ as

$$\mathbf{v}_{ns} = \mathbf{v}_n - \mathbf{V}_s \tag{7}$$

and $\mathbf{V}$ as its average

$$\mathbf{V} = \overline{\mathbf{v}_{ns}} \ . \tag{8}$$

In general the superfluid velocity $\mathbf{v}_s$ contains more contributions than $V_s$ alone [Eq. (1)], so $\mathbf{v}_{ns}$, introduced in Eq. (7), is not the local difference in the velocities of the normal and the superfluid components, which is $\mathbf{v}_n - \mathbf{v}_s$.

### B. The local approximation

The integral in Eq. (4) can be split in a local and a nonlocal contribution. The local contribution results from the sections of the line (adjacent to the excluded regions of length $\delta$) where the vortex can be approximated by circle segments. The local term is given by

$$\mathbf{v}_l = \frac{\kappa \ln(R/a_0)}{4\pi} \mathbf{s}' \times \mathbf{s}'' \tag{9}$$

with $\mathbf{s}' = d\mathbf{s}/d\xi$, $\mathbf{s}'' = d^2\mathbf{s}/d\xi^2$, and $R = 1/|\mathbf{s}''|$ is the local radius of curvature.

The nonlocal term represents the contribution from the rest of the vortex line. Usually the local contribution is an order of magnitude larger than the nonlocal one, so the latter can be neglected (local approximation). By multiplying the local term with a constant $c$ somewhat larger than 1 the influence of the nonlocal contribution can be taken into account to some extent. By comparing the self-induced velocity in the local approximation with a fully nonlocal approximation in a typical tangle we obtained $c = 1.1$. All our calculations were performed in this modified local approximation. In that case

$$\mathbf{v}_i = \beta \mathbf{s}' \times \mathbf{s}'' \tag{10}$$

with

$$\beta = c(\kappa/4\pi)\ln(R/a_0) \ . \tag{11}$$

This definition of $\beta$ is slightly different from the one introduced by Schwarz, who took $\beta = (\kappa/4\pi)\ln(cR/a_0)$, with $c$ a constant of order 1.[4]

The $\mathbf{v}_b$ term in Eq. (1) can be regarded as a nonlocal contribution, so in the local approximation

$$\mathbf{v}_b = 0 \tag{12}$$

leading to

$$\mathbf{v}_s = \mathbf{V}_s + \beta \mathbf{s}' \times \mathbf{s}'' \tag{13}$$

for Eq. (1). Equations (3) becomes

$$d\mathbf{s}/dt = \mathbf{V}_s + \beta \mathbf{s}' \times \mathbf{s}'' + \alpha \mathbf{s}' \times (\mathbf{v}_n - \mathbf{V}_s - \beta \mathbf{s}' \times \mathbf{s}'') \ . \tag{14}$$

In principle, all variables in (14) are functions of the parameter $\xi$. In the numerical calculations the vortex lines are represented by an array of $N_p$ discrete points $i$ at positions $\mathbf{s}_i$. Equation (14) then obtains the form

$$d\mathbf{s}_i/dt = \mathbf{V}_s + \beta_i \mathbf{s}_i' \times \mathbf{s}_i'' + \alpha \mathbf{s}_i' \times (\mathbf{v}_n - \mathbf{V}_s - \beta_i \mathbf{s}_i' \times \mathbf{s}_i'') \ . \tag{15}$$

Also the velocity $\mathbf{v}_n$ has to be evaluated in $\mathbf{s}_i$. In our calculations Eq. (15) is solved with a stable and accurate Crank-Nicolson algorithm using iterations.[9,10] This algorithm is stable even in the case of zero mutual friction. It can be shown analytically[10] that the Crank-Nicolson method with two iterations is stable when the time step $\Delta t$ satisfies the condition $\Delta t < a^2/(4\beta)$, where $a$ is the minimum distance between two neighboring points $\mathbf{s}_i$ and $\mathbf{s}_{i+1}$ on the discretized vortex line. The stability of the scheme was tested by numerically calculating the motion of vortex rings, ellipses, and many other vortex arrangements. In contrast with Schwarz, who used a fixed time step, the calculation speed was significantly optimized by using a variable time step according to the condition given above.

The line-length density $L$ of a vortex tangle in a volume $\Omega$ is given by

$$L = \frac{1}{\Omega} \int d\xi \ . \tag{16}$$

The time average of $L$ will be denoted by $\Lambda$; the reverse average line distance $\Lambda^{1/2}$ by $\lambda$. The density of the force exerted by the normal component on the superfluid component, the average mutual-friction force density $F$, is calculated from the relation

$$\mathbf{F} = -\frac{\alpha \rho_s \kappa}{\Omega} \overline{\int \mathbf{s}' \times [\mathbf{s}' \times (\mathbf{v}_n - \mathbf{v}_s)] d\xi} \ . \tag{17}$$

It is related to the gradient in the $^4$He molar chemical potential through

$$\nabla \mu_4 = -M_4 \mathbf{F}/\rho_s \ , \tag{18}$$

where $M_4$ is the $^4$He molar mass and $\rho_s$ is the superfluid density. The reduced average mutual friction force density is defined as

$$\Gamma = F/\rho_s \kappa V \ . \tag{19}$$

With Eq. (18), $\nabla \mu_4$ can be written as

$$\nabla \mu_4 = -\kappa M_4 \Gamma V \ . \tag{20}$$

For an isotropic tangle, $F$ and $L$ are related as follows:

$$F = \tfrac{2}{3} \alpha \kappa \rho_s V L \ . \tag{21}$$

The factor $\frac{2}{3}$ reflects the isotropic character of the tangle.[5]

### C. Reconnections

When two antiparallel vortex segments approach they will reconnect[11] due to the nonlocal interaction. This effect is suppressed in the local approximation. A parameter

$$\Delta_i = 2R_i/[c \ln(R_i/a_0)] , \tag{22}$$

with $R_i$ the radius of curvature in point $i$, is introduced which is the distance where the velocity due to an infinitely long vortex line is equal to the local velocity. Typically $\ln(R_i/a_0)$ is of order 10. In the calculations a reconnection between two points $i$ and $j$ was enforced whenever the distance $|\mathbf{s}_i - \mathbf{s}_j|$ between two points $i$ and $j$ satisfied the condition

$$|\mathbf{s}_i - \mathbf{s}_j| < \min(\Delta_i, \Delta_j) . \tag{23}$$

In order to trace a pair of points that satisfy condition (23) a sorting formalism was used, which typically needed $N_p \ln(N_p)$ calculations. It is described in detail in Ref. 10.

In a similar way a vortex was connected to the wall whenever a point $i$ approaches it within a distance

$$\Delta_w = R_i/[c \ln(R_i/a_0)] . \tag{24}$$

The average $\Delta_w$ determines the size of the boundary layer, which plays a key role in the nonlinear and critical velocity effects in $^4$He II.

### D. Dimensional considerations

Through the $\ln(R/a_0)$ dependence the parameter $\beta$ depends weakly on the radius of curvature. In the following discussion we take a typical value of $R$ in the expression for $\beta$, which is treated as a constant. Strictly speaking the radius of curvature $R$ is a property, which is the result of the equation of motion. The truly independent variables in Eq. (14) are the velocity $\mathbf{V}$, the vortex strength $\kappa$, and the core diameter $a_0$. In confined geometries also the size of the flow channel enters into the expressions. The following dimensionless quantities are introduced: The position vector

$$\sigma = \mathbf{s}V/\beta , \tag{25}$$

time

$$\tau = tV^2/\beta , \tag{26}$$

velocity difference

$$\varphi_{ns} = \mathbf{v}_{ns}/V , \tag{27}$$

and the dimensionless superfluid velocity

$$\varphi_s = \mathbf{V}_s/V . \tag{28}$$

Equation (14) in dimensionless form then reads

$$d\sigma/d\tau = \varphi_s + \sigma' \times \sigma'' + \alpha\sigma' \times (\varphi_{ns} - \sigma' \times \sigma'') . \tag{29}$$

The dimensionless reversed average line-length distance $\lambda_0$ is given by

$$\lambda_0 = \beta\lambda/V . \tag{30}$$

## III. RESULTS

### A. Square cross section

As a first case we discuss the calculated flow properties of a square capillary with edges $d = 50$ $\mu$m assuming pure normal-fluid plug flow ($\mathbf{V}_s = 0$ and $\mathbf{v}_n = \mathbf{V}$). In first instance the length $l$ of the period of the periodic boundary conditions was also 50 $\mu$m, so the calculations were applied to a cubical control volume of $50 \times 50 \times 50$ $\mu$m$^3$. Figure 2(a) represents the starting situation, which consisted of 13 rings, chosen in such a way that there were no immediate reconnections, and that the average self-induced velocity in the $z$ direction was zero.

Figure 2(b) shows the vortex tangle, which developed from this starting situation after 38 ms for $V = 118$ mm/s. Except for the boundary layer, the vortex lines are homogeneously distributed over the channel as may be expected from the flat profile. Figure 3 shows the line-length density $L$ as a function of time. After a transient period a dynamical equilibrium was reached in which $L$ fluctuates around an average value of about 0.009 $\mu$m/$\mu$m$^3$. However, when $V$ was decreased to a value below $100 \pm 2$ mm/s the vortex tangle was not self-sustained, and $L$ tended to zero. In our definition this means that the critical velocity $V_c$ of this channel is 100 mm/s.

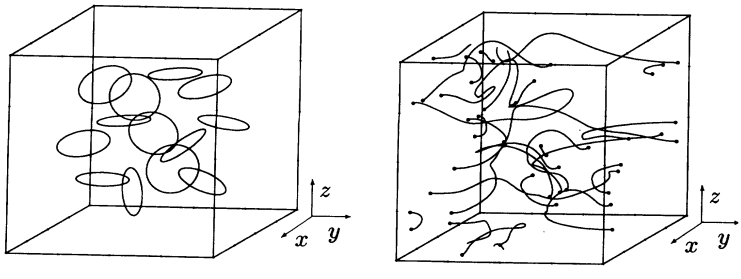


(a) (b)

FIG. 2. (a) The 13 rings, which formed the starting situation for many of the simulations. (b) Vortex tangle, which evolved from the ringes of (a) for $V = 118$ mm/s, in a square channel [Fig. 1(a)] after 38 ms. The dots mark the points where the lines touch the walls.

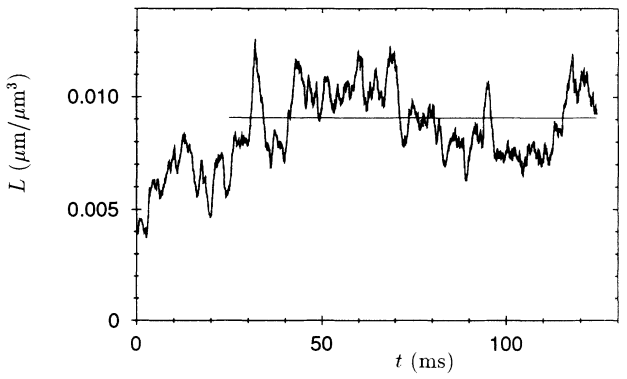


FIG. 3. The line density $L$ as a function of time for $V=118$ mm/s for the tube with a square cross section and normal-fluid plug flow. The horizontal line indicates the time average for the time interval between 25 and 124 ms.

Figure 4(a) represents the calculated $\lambda$-$V$ dependence. It is in good approximation linear in $V$ so we introduce

$$\lambda=\gamma_L(V-v_{L0}) , \tag{31}$$

where $\gamma_L$ and $v_{L0}$ are parameters, which in this case are equal to 1.3 s/mm$^2$ and 47 mm/s, respectively.

Due to the periodic boundary conditions the calculated local line-length density cannot vary over length scales larger than $l$. Variations in the line density over larger length scales are suppressed. This may affect the results. Therefore, the average flow properties have been determined also for $l=2d$ and $4d$. Examples of typical tangles are presented in Fig. 5. Figure 4 shows that $V_c$ increases slightly with $l$. For $l=4d$ we obtained $V_c=108\pm2$ mm/s or

$$V_c=60\beta/d . \tag{32}$$

The jump in $\lambda$ at $V_c$ decreases with $l$. Probably the transition may be continuous for very long capillaries. For $V\gg V_c$ the dimensionless reversed average line distance $\lambda_0$ is expected to be constant. In this case $\lambda_0=0.112$.

In Fig. 4(b) $\sqrt{\Gamma}$ is plotted as a function of $V$. For $l=d$ the $\sqrt{\Gamma}-V$ relationship is fairly linear, so we introduce

$$\sqrt{\Gamma}=\gamma_F(V-\mathbf{v}_{F0}) , \tag{33}$$

where $\gamma_F$ and $\mathbf{v}_{F0}$ are parameters, which in this case are equal to 0.35 s/mm$^2$ and 45 mm/s, respectively.

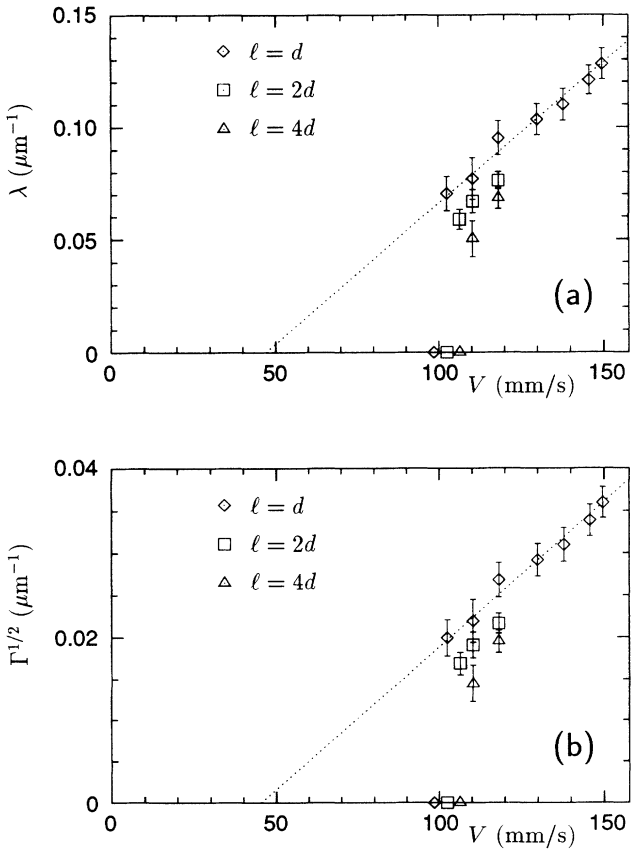


FIG. 4. Flow properties of the square channel plotted as functions of $V$. Points for three different periodicity lengths $l$ are presented. The lines are linear fits to the data for $l=d$. The error bars represent the standard deviation. (a) The inverse average line distance $\lambda$. (b) The square root of the reduced mutual friction force density $\Gamma$.

### B. Circular channels

For the capillaries with a circular cross section four different cases were investigated: pure normal *Poiseuille* flow ($\mathbf{V}_s=0$, $\mathbf{V}_n=\mathbf{V}$), thermal *counterflow* (at $T=1.6$ K: $\mathbf{V}_s=-0.16\mathbf{V}$, $\mathbf{V}_n=0.84\mathbf{V}$), "*combined flow*," which in this paper is defined as the flow situation, where the average normal and superfluid velocities are equal in size but with opposite directions ($\mathbf{V}_s=-0.5\mathbf{V}$, $\mathbf{V}_n=0.5\mathbf{V}$), and, finally, pure normal-fluid *plug flow* ($\mathbf{V}_s=0$, $\mathbf{v}_n=\mathbf{V}_n=\mathbf{V}$). As was mentioned earlier, the latter case also corresponds with *pure superflow* ($\mathbf{V}_s=-\mathbf{V}$, $\mathbf{v}_n=0$).

Figure 6(a) shows a typical tangle for plug flow for $V=118$ mm/s. The general behavior of the time dependencies of $L$ and $F$ is the same as for the square capillary. Also the $\lambda$-$V$ dependencies for $l=d$ are practically the same. Figure 6(b) is a typical example of a tangle for pure normal flow with a *parabolic* flow profile. It is distinctly different from the plug-flow case: The vortex lines are pushed towards the walls, leaving a low line density in the center. This is in agreement with the results of Samuels[12] who showed that vortex rings tend to take a position in a region in the tube, where the relative velocity of the normal and the superfluid components is zero. In this case this position is at the wall of the channel.

Figure 7(a) presents the $\lambda$-$V$ dependencies for $l=d$ for normal-fluid plug flow and for parabolic flow. Within the accuracy the values of the critical velocities are the same, but the slopes of the $\lambda$-$V$ dependencies differ significantly. The results of simulations with $l=2d$ were not significantly different from the $l=d$ case. Figure 7 also contains the results for thermal counterflow. They are positioned in between the two previous cases.

The spatial properties of the tangles are treated in more detail in Fig. 8, where six time-averaged properties of the tangle are plotted as functions of the radius $r$ for normal-fluid plug flow, pure normal Poiseuille flow, and

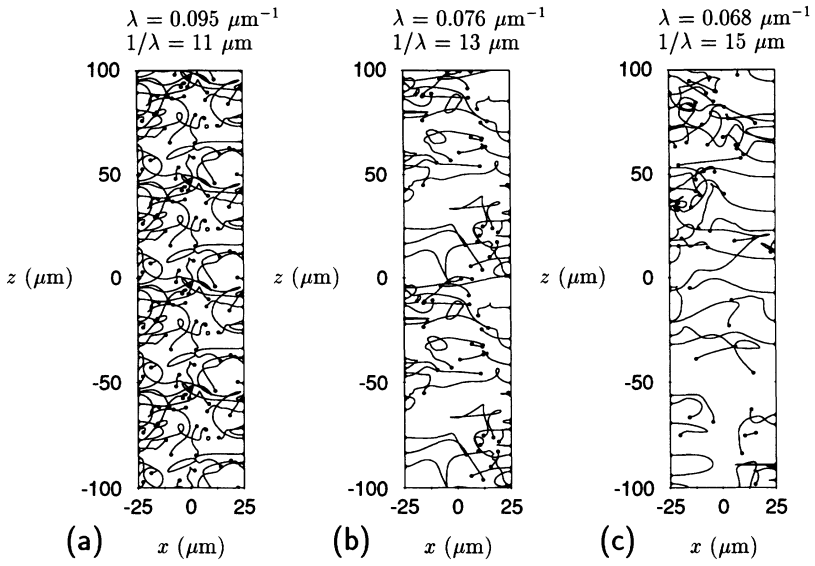


FIG. 5. Tangles for $V=118$ mm/s ($Vd/\beta=66$) in a tube with a square cross section of $50\times50$ $\mu$m$^2$. In the plots the total length of the tube section is the same, but the periodicity length is different: (a) $l=50$ $\mu$m, (b) $l=100$ $\mu$m, and (c) $l=200$ $\mu$m. The differences in line densities between the three cases are clearly visible.

for combined flow respectively. For plug flow $\Lambda$ is homogeneous in the major part of the capillary [Fig. 8(a)]. Near the wall $\Lambda$ decreases. This is due to the reconnections with the wall, which take place in the boundary layer, which has a thickness of about 4 $\mu$m. In this region the vortices are oriented mainly perpendicular to the surface.

Figure 8(b) represents the time average of the number $n$ of vortex lines penetrating a surface of unit area, oriented in the radial direction. For a flat normal profile $n$ is equal to zero. For the other profiles $n$ has a typical value of 0.002 vortices per $\mu$m$^2$, or about 2.5 vortices in an area of $25\times50$ $\mu$m$^2$. We will come back to the physical significance of this nonzero $n$ in the discussion.

Figure 8(c) shows the distribution of the axial component of the mutual-friction force density. In all cases the force is constant except for the region close to the wall. The values correspond to pressure gradients of typically 1000 Pa/m. In pure normal Poiseuille flow the viscous pressure gradient is 1900 Pa/m.

Figure 8(d) shows that $\mathbf{F}$ has a radial component,

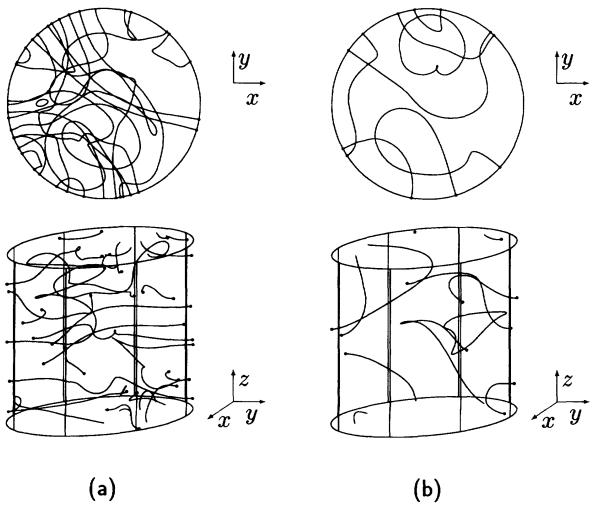


FIG. 6. Vortex tangles in a tube with a circular cross-section with pure normal flow for $V=118$ mm/s. (a) Plug flow, situation after 153 ms and (b) parabolic profile, situation after 163 ms.

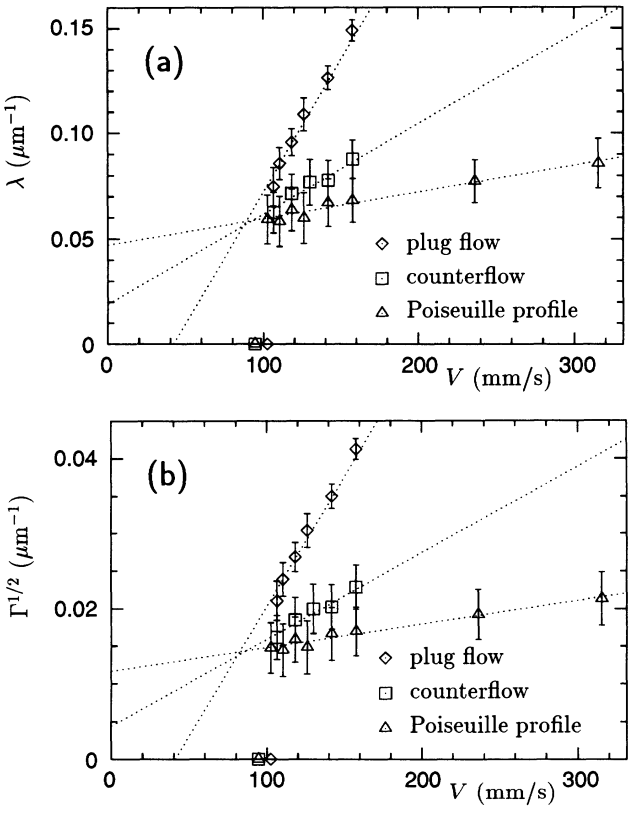


FIG. 7. Velocity dependencies of flow properties of circular tubes. In all data points $l=d=50$ $\mu$m. Results for normal-fluid plug flow, for counterflow, and for a parabolic normal flow profile are shown. The lines represent Eq. (31) and Eq. (33), fitted to the data for $V>V_c$. (a) The average reversed line distance $\lambda$ and (b) the square root of the reduced mutual-friction force density $\Gamma$.

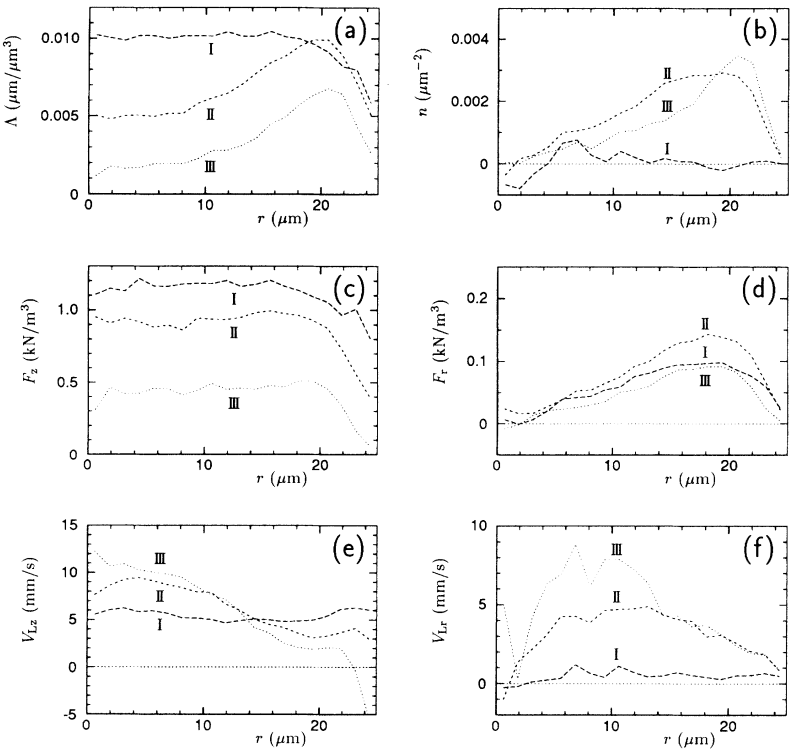


FIG. 8. Calculated properties of the tangles as functions of the radius for a circular capillary with $d=50$ μm and $V=118$ mm/s. In all plots the results are shown for (I) plug flow, (II) combined flow, and (III) Poiseuille flow. The plots represent the $r$ dependence of the time averages of (a) the line-length density $\Lambda$, (b) vortex number density $n$, (c) mutual-friction force density in the axial direction $F_z$, (d) mutual-friction force density in the radial direction $F_r$, (e) vortex velocity in the flow direction $V_{Lz}$, and (f) vortex velocity in the radial direction $V_{Lr}$.

which is typically 10% of the axial component. The reaction force on the normal component will drive it towards the center of the tube. In the stationary state this effect has to be balanced somehow.

Finally, Figs. 8(e) and 8(f) give the velocities of the discretization points on the vortex lines as calculated with Eq. (15). The positive values of $V_{Lr}$ mean that the points move towards the wall. For a correct interpretation of this result one should keep in mind that the velocity of a discretization point has some arbitrariness. It is permitted to add a component in the tangential direction (i.e., the direction of $\mathbf{s}'$) to it. Therefore the velocities presented in Figs. 8(e) and 8(f) cannot simply be interpreted as *the* velocities of the vortex lines.

In Fig. 9 the ratio $3\Gamma/(2\alpha L)$ is plotted. For an isotropic tangle it should be equal to 1. The deviations are on the order of 15%. Equations (18) and (21) are often used to derive line densities from experiment. The fact that the tangles are anisotropic introduces errors of typically 15% in the quoted average line densities.

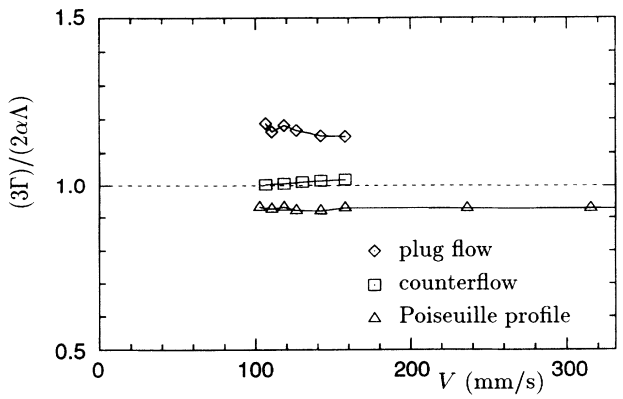


FIG. 9. The anisotropy parameter $3\Gamma/2\alpha\Lambda$ for three different flow situations as functions of $V$ in tubes with a circular cross section. The dotted horizontal line indicates the value one, which corresponds with an isotropic tangle.

### C. Infinitely wide slit

In the case of an infinitely wide slit periodic boundary conditions were applied in the $z$ and $y$ directions [Fig. 1(c)]. The periodicity lengths were 50 μm. The width of the slit was 50 μm, so the control volume again was $50\times50\times50$ μm$^3$. The calculations were started with the 13 rings as in the previous cases.

First we discuss the results of normal-fluid plug flow as shown in Fig. 10. In the first 50 ms a tangle develops similar to the ones discussed before. In a later stage, however, the tangled structure disappears. In the final situation a number of straight vortex lines in the $x$ direction are moving with velocity $\alpha V$ [in Eq. (15) $\mathbf{V}_s$ and $\mathbf{s}''$ are zero] in the $y$ direction. The number of positively oriented lines is equal to the number of opposite lines so half of the lines move in the positive $y$ direction and the other half in the negative $y$ direction. The drag force per unit line length [Eq. (17)] is $\alpha\rho_s\kappa V$, so if there are $N_v$ vortices in the control volume of edge $d$ the number density $n=N_v/d^2$ and the mutual friction force density is given by

$$\mathbf{F}=\alpha n\rho_s\kappa\mathbf{V} \ . \tag{34}$$

The average mutual-friction force density depends on the

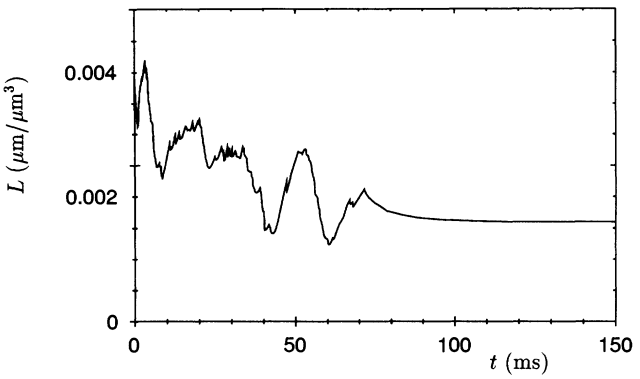


FIG. 10. Time dependence of $L$ for $V=47$ mm/s in the slit ($d=50$ $\mu$m and $l=50$ $\mu$m). The tangle degenerates after about 75 ms. In this case there were two pairs of noninteracting straight vortex lines in the control volume in the final situation.

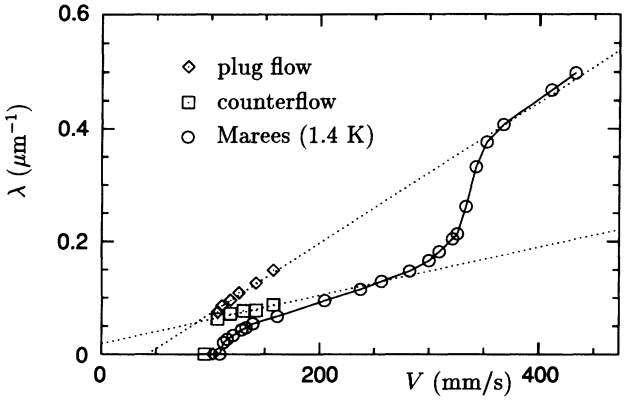


FIG. 11. Inverse averaged line distance $\lambda$ as a function of $V$. This plot shows the calculated results for a plug flow and Poiseuille flow together with the scaled (see the text) measured points of Marees and van Beelen (Ref. 18).

number of vortex lines in the final situation, which was in our case of order 1. Only after averaging over a large number of different starting conditions, or by taking a large control volume, sufficient statistics can be obtained to define an average line density. In any case $F$ tends to a finite value at every value of $V$, so $V_c=0$. We will come back to this result in the discussion.

If a *parabolic* normal velocity profile was assumed the tangle degenerated into a set of slightly curved vortex lines. In the final situation the lines lie in a plane making an angle $\arctan(\alpha)$ with the $z$ direction. For $\alpha V d/\beta \ll 10$, and neglecting terms of order $\alpha^2$, the curves can be approximated by the equation

$$\mathbf{s}(x)=(x,-\alpha z,z) \tag{35}$$

with

$$z=\frac{\alpha V d^2}{4\beta}\left[-\frac{x^2}{d^2}+2\frac{x^4}{d^4}\right]. \tag{36}$$

Just as in the case of a flat normal-velocity profile the vortices move in the $y$ direction with velocity $\alpha V$.

## IV. COMPARISON WITH EXPERIMENT

During the past many decades the flow properties of He II have been determined experimentally. The properties have been mapped in the $V_s$-$V_n$ plane, which shows a rich structure with various turbulent regimes, separated by critical velocity lines.[13] The properties are temperature, size, and geometry dependent. Also the condition of the surface of the flow channel is of importance.

In the comparison with experiment we first discuss thermal counterflow. This is widely investigated experimentally.[1,2,14–21] In round capillaries two critical velocities are found experimentally: $V_{c1}$ and $V_{c2}$.

The main results of our calculations are summarized in Fig. 7, where $\lambda$ and $\sqrt{\Gamma}$ are plotted as functions of $V$. In order to compare these with experiment we plotted in Fig. 11, as an example, the experimental results of Marees and van Beelen[18] together with our calculated results for the parabolic and the flat profile. Unfortunately the experimental and the calculated results apply to capillaries with different diameters (216 $\mu$m and 50 $\mu$m, respectively), and different temperatures (1.4 K and 1.6 K, respectively). Therefore the experimental results were scaled. In accordance with Eq. (25) the velocity scale was multiplied with a factor $216/50=4.32$, correcting for the difference in diameters, and divided by 1.13 accounting for the different $\beta$ values. This resulted in $V_{c1}=110$ mm/s, which agrees with the calculated value of 100 mm/s. The $\lambda$ scale was multiplied with a factor 4.32 of the diameter ratio, and reduced with an additional 20% so that the experimental $\lambda$-$V$ curve in the high-velocity region fits calculated result of plug flow. Although it probably is somewhat suggestive to compare the experimental and calculated results in this way, the general picture from Fig. 11 is that $V_{c1}$ is a transition to a turbulent state in the superfluid component, keeping the normal-component velocity profile in tact (i.e., parabolic), while $V_{c2}$ marks a transition in the normal component velocity profile from parabolic to flat. This has also been suggested by Tough[1] and Donnelly.[2] Awschalom, Milliken, and Schwarz measured $\Lambda$ and $v_n$ as functions of the positions in a $1\times2.5$ cm$^2$ rectangular channel.[22] They reported constant values of $\lambda$ and $v_n$. It should be noted that in this experiment, at the lowest value of the velocity $V=2.7$ mm/s, the average line spacing was 0.27 mm, which is well below the typical channel size, so their measurements applied to the fully turbulent state.

Experimentally it is found that the parameter

$$a=\frac{V}{V_n}\left[1-\frac{\Lambda}{\Lambda_s}\right] \tag{37}$$

(Refs. 19 and 20) with $\Lambda_s$ the average line length density for pure superflow, is a constant equal to 0.95 at 1.6 K. As can be derived from Fig. 12 (keeping in mind that pure superflow is equivalent with pure normal-fluid plug flow) the calculated value of $a$ is velocity dependent, although the order of magnitude is correct. The agreement

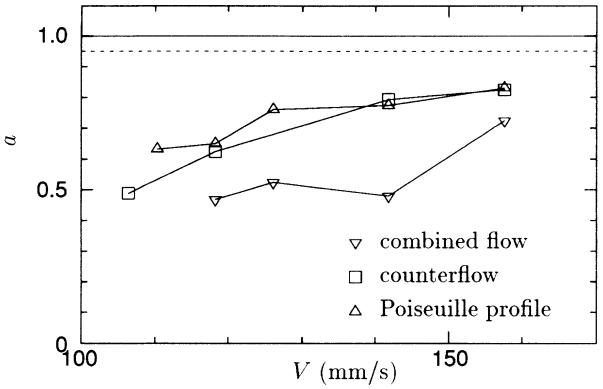


FIG. 12. Calculated $a$ values [Eq. (37)] as functions of $V$. The points represent plug flow, counterflow, and combined flow. The experimental value of 0.95 is indicated with the horizontal dashed line.

with experiment improves when in Eq. (37) the $\Lambda_s$ values for $\lambda=4d$ are substituted.

In Table I, values for the parameters $\gamma_L$, $v_{L0}$, $\gamma_F$, $v_{F0}$, and $V_c$ are presented for $d=l=50$ $\mu$m. The ratio of $\gamma_L$ for plug flow and Poiseuille flow is about one-third. In the counterflow experiments of Martin and Tough[21] and of Marees, van der Slot, and van Beelen[23] $\gamma_L$ in the $T$ I state is about half the value in the $T$ II state.

Table II summarizes the calculated and measured scaled critical velocities $V_{c1}d/\beta$ and $V_{c2}d/\beta$ at 1.6 K from different sources. The results of our calculations on $V_{c1}$ and $\lambda_0$ typically deviate 20% of the results of Schwarz, which is reasonable in view of the difference in algorithm. In the analysis of experimental data the value of $\beta$ is determined using the expression

$$\beta=\frac{c\kappa}{4\pi}\ln(\delta_\beta\lambda)\ . \tag{38}$$

This expression is based on the assumption that $\delta_\beta\lambda$, with $\delta_\beta=0.15$ nm, is a good representation for the typical $R/a_0$ value of a tangle.[4] If necessary the value of $\lambda$ is estimated using the relations[1] $\lambda d=2.5$ at $V_{c1}$ and $\lambda d=20$ at $V_{c2}$. Table II shows that there is reasonable agreement with our value of $V_c d/\beta=60$ and the experimental values for $V_{c1}d/\beta$, which are in the rather wide range of 22–95. In any case it is considerably lower than the typical values found for $V_{c2}$, which is in the 120–200 range.

The fact that the critical velocities in circular and square tubes are the same is confirmed by the experiments of Henberger and Tough who observed that the square tubes "appear to be essentially identical to circular tubes."[24] Marees and van Beelen[18] measured that $V_c$ for counterflow and for pure superflow both are temperature dependent. At about 1.6 K he found that the two critical velocities are equal, which agrees with our calculations. This may imply that the calculated result that $V_c$ for pure normal-fluid plug flow is the same as for Poiseuille flow is not generally true but somewhat accidental. It may only be true at the particular value of $\alpha=0.1$, which was chosen in our calculations.

The ratio of the effective $^3$He density and the total fluid density for a saturated mixture at very low temperatures is $(m^*/m_3)(\rho_3/\rho)=2.46\times7.05/140=0.12$ (Ref. 25). A $\rho_n/\rho$ value of 0.12 for pure $^4$He corresponds with a temperature of 1.5 K. So, presumably, the experimental results for mixtures at very low temperatures are also described by our calculations for pure $^4$He at 1.6 K. Zeegers *et al.* measured the critical velocities of $^3$He, and chemical potential differences, in $^3$He-$^4$He mixtures for many capillaries.[26] For $d=50$ $\mu$m they found $V_c=120\pm50$ mm/s, which agrees remarkably well with the calculated value of 100 mm/s. The general character of the $\sqrt{\Delta\mu/lV}$-$V$ dependencies [see, e.g., Fig. 10(b) of Ref. 26, please note that the parameters $\alpha$ and $\Gamma$ in Ref. 26 are different from the ones used here] resemble the $\sqrt{\Gamma}$-$V$ relationships calculated here. The slope of the measured curves corresponds with $\gamma_F=0.5$ s/mm$^2$, which is close to the value of 0.35 s/mm$^2$ found for normal-component plug flow (Table I). This is somewhat surprising as the measured pressure drop across the flow channel is consistent with the Poiseuille flow. Satoh and Okuyama,[27] who used NMR to study adiabatic flow, showed that the normal-component velocity profile just above the first critical velocity is parabolic.

## V. DISCUSSION

### A. Critical velocities

The boundary layer $\Delta_w$ is defined by Eq. (24), with a typical value for $R$. The processes in the boundary layer are different from the processes in the bulk: The vortex lines are oriented perpendicular to the wall; the radius of curvature is relatively small. There are many small semicircular vortex rings [Fig. 2(b) and Fig. 13(b), the latter

TABLE I. Values for the parameters $\gamma_L$, $v_{L0}$, $\gamma_F$, $v_{F0}$, and $V_c$ for the geometries that are discussed in this paper. In all simulations the typical length scale $d=50$ $\mu$m. Only values of "short" tubes ($l=d$) are tabulated.

| Geometry | Flow type | $V_n$ | $\gamma_L$ (s/mm$^2$) | $\gamma_F$ (s/mm$^2$) | $v_{L0}$ (mm/s) | $v_{F0}$ (mm/s) | $v_c$ (mm/s) |
|---|---|---|---|---|---|---|---|
| Slits | Plug | $V$ | 1.1 | 0.29 | 0 | 0 | 0 |
| Square | Plug | $V$ | 1.3 | 0.35 | 47 | 45 | 100 |
| Circular | Plug | $V$ | 1.3 | 0.35 | 42 | 41 | 100 |
| Circular | Combined | $0.5V$ | 0.87 | 0.25 | 17 | 21 | |
| Circular | Counterflow | $0.16V$ | 0.43 | 0.12 | $-40$ | $-40$ | 100 |
| Circular | Poiseuille | 0 | 0.13 | 0.031 | $\approx-370$ | $\approx-370$ | 100 |

TABLE II. Values for the scaled critical velocities $V_{c1}d/\beta$ and $V_{c2}d/\beta$ from different sources at $T=1.6$ K. The parameter $\lambda_0$ is calculated from the $\Lambda(V)$ dependence for $V > V_{c2}$. The first two lines of this table lists the results of numerical simulations for plug flow. The second part is from an analysis of data from counterflow experiments.

| Source | Tube geometry | $d$ ($\mu$m) | $V_{c1}d/\beta$ | $V_{c2}d/\beta$ | $\lambda_0$ |
|---|---|---|---|---|---|
| This work | Square and circular | 50 | 60 | | 0.112 |
| Schwarz (Refs. 3 and 5–7) | Square and circular | | 48 | | 0.137 |
| Brewer and Edwards (Ref. 32) | Circular[a] | 366 | | 200 | 0.131 |
| | | 108 | 67 | 200 | 0.122 |
| | | 52 | 51 | | |
| Childers and Tough (Ref. 33) | Circular | 126 | 49 | | |
| | Circular | 61 | 22 | | |
| Henberger and Tough (Ref. 24) | Square | 120 | 54 | 120 | |
| Martin and Tough (Ref. 21) | Circular | 1000 | 95 | 200 | 0.122 |
| Swanson and Donnelly (Ref. 34) | Square | 10000 | | 200 | |
| Marees, van der Slot, and van Beelen (Ref. 23) | Circular | 130 | 38 | | |
| Courts and Tough (Ref. 35) | Circular | 134 | 44 | | |
| Courts and Tough (Ref. 20) | Circular | 134 | | 200 | 0.157 |

[a] $T=1.563$ K.

also represents the projection of a typical tangle] moving with high speed in some cases even in a direction opposite to the applied flow [Fig. 8(e)]. As can be seen in Fig. 8(a) the line length density is lower near the wall than in the bulk. For velocity values just above $V_c$, in the central regions of the tube, the tangle consists of slowly moving vortex lines with radii of curvature which typically are on the order of the channel size.

In normal-fluid plug flow $\mathbf{V}=\mathbf{V}_n$, $\varphi_s=0$, and $\varphi_{ns}=\mathbf{e}_z$. Based on Eqs. (29) alone, this would imply that, e.g., $\lambda$ is proportional to $V$, and that $\lambda$ is independent of the size of the flow channel. However, the thickness of the boundary layer $\Delta_w$ scales with $\beta/V$, so the relative importance of the boundary layer increases with decreasing $V$. This is illustrated in Fig. 13. Figure 13(a) represents a tangle in a square channel with edges $d$; the normal velocity is $V$. Figure 13(b) represents a situation where the velocity $V$ is reduced, e.g., by a factor of 2 and the tube and the tangle are expanded with the same factor [Fig. 13(b)]. In that case the typical radius of curvature, and the resulting thickness of the boundary layer [Eq. (24)], also increase with a factor of 2 (again neglecting the weak logarithmic $R$ dependence of $\beta$). The time evolutions of the tangles in the small [Fig. 13(a)] and the large channel [Fig. 13(b)] will be practically identical if the time scale in the large channel is four times larger [Eq. (26)]. However, if walls are put into the channel of Fig. 13(b), resulting in the four separate channels represented in Fig. 13(c), the total area covered by the boundary layers is increased. The channel in Fig. 13(a) is the same as one of the channels in Fig. 13(c), but, due to the increased influence of the boundary layer, the two situations are essentially different. The evolution of the tangle, and the resulting $\lambda$, will be different. In fact, $\lambda$ in the case of Fig. 13(c) will be smaller then the reduction of the factor of 2 obtained from the scaling according to Eq. (25) because the line density near the walls is low. So reducing $V$ by a factor of 2, while keeping the tube dimension constant, leads to a reduction of $\lambda$ of more than a factor of 2. This is the basic reason for the phenomenon of critical velocities in He II flow: By reducing the velocity from some high value, $\lambda$ will decrease stronger than linear with $V$. At some specific value $V_c$ of $V$ the value of $\lambda$ drops to zero. So the critical velocity is due to the specific properties of the boundary layer. This is reminiscent to the assumptions made in the pioneering work of Vinen.[27]

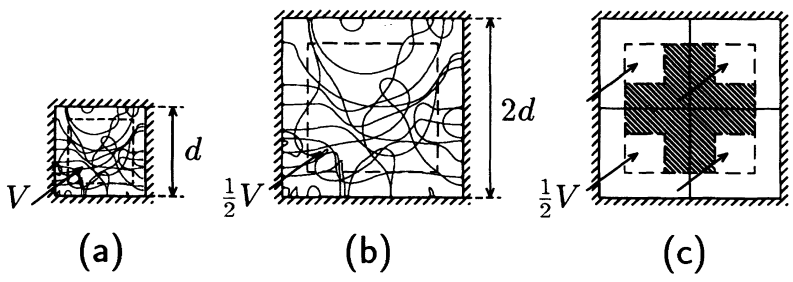


FIG. 13. (a) Schematic representation of a vortex tangle in a square channel with applied velocity $V$. The dashed lines indicate the boundary layer. (b) Same tangle as in Fig. 13(a), but now the dimensions (including the boundary layer) are twice as large and the applied velocity is half. On a four times larger time scale the evolution of this tangle will be the same as in Fig. 13(a). (c) Same situation as in Fig. 13(b), but now walls divide the channel in four channels of the same size as in (a). The evolution will be different from the evolution in (b), and consequently also from Fig. (a), due to the added walls.

As argued above the tangle properties depend on the channel size even in the case of normal-fluid plug flow or pure superflow. In the presence of a parabolic normal-flow profile this effect adds up to the variations of $v_n$ with the typical length scale ($d$) of the channel [Eq. (5)]. The flow phenomena do not scale simply as $Vd/\beta$.[28] Within the (relatively large) scatter in the points Zeegers *et al.*[25] found a linear $V_c d$-ln($d$) dependence, but the line extrapolated to $V_c d = 0$ for $d = 15$ $\mu$m, instead of a value on the order of $a_0$, which would be expected if $V_c d$ is proportional to $\beta$.

In this paper the critical velocity is defined as the velocity value above which the vortex tangle is permanently sustained by the externally applied flows. This picture is very appealing but incomplete. Due to the application of periodic boundary conditions in fact an infinite number of vortex rings was initially put into the infinitely long channel. In a channel of finite geometry the tangle will be flushed away from the channel even at velocities above critical. Some additional mechanism is needed to explain the observation of steady mutual friction in finite channels. Schwarz[7] proposed a mechanism in which a "vortex mill" from remanant vortices near the tube entrance produces turbulence which downstream develops into a tangle. Also the creation of vortices can explain the observed steady state. Figure 8(e) shows that the drift velocity of the vortex lines in our case was typically 5 mm/s. So it takes 10 ms to travel through the control volume of 50 $\mu$m length. With typically 5–10 rings in the control volume a production rate near the tube entrance of 10 rings per 10 ms would be sufficient for the case of pure normal flow. In the case of pure superfluid flow the drift velocity of the vortices is about equal to $V$, which is on the order of 100 mm/s. In that case the creation frequency should be an order of magnitude higher.

Samuels[12] has shown that vortices tend to arrange in rings in the regions of zero relative velocities. This interesting case does not apply to our situations. In all our simulations the velocities of the normal and the superfluid components were opposite, so a region of zero relative velocity does not exist in the fluid. In the special case of $V_s = 0$ this region is positioned at the wall of the tubes, where both $v_n$ and $V_s$ are zero. However, here the interactions with the wall, which were neglected by Samuels, play a dominant role.

For slits the numerical results produce a zero critical velocity. This agrees with the experimental results of Zeegers *et al.* for an annular spaces[26] and the results of Ladner and Tough,[30,31] and Henberger and Tough,[24] who found a reduced critical velocity in a rectangular channel with high aspect ratio. However, this agreement can be fortuitous. It is possible that the calculated zero critical velocity is an artifact of using the local approximation. In the final situation the vortex lines are fairly straight so the motion of a vortex line is affected by the (nonlocal) velocity fields of the other vortices. In the presence of mutual friction this can lead to vortex annihilation. So the critical velocity may be nonzero after all. The model has to be extended with nonlocal contributions before definite conclusions can be drawn.

### B. Self-consistent flow profiles

In our calculations the flow profiles of the normal and the superfluid components were imposed to be parabolic and/or flat. In reality only the mass flows are determined by the experimentalist and the flow profiles *result* from the viscous stresses, the slip condition at the wall, and the interactions between the two components (mediated by the vortices). In principle, the shape of the profiles has to be derived from a self-consistent calculation.

The two cases with parabolic normal-flow profiles described in Fig. 8(b) show a maximum in $n$ at about 5 $\mu$m from the wall. This is due to the fact that the tangle tends to organize in circles around the capillary axes. This leads to a macroscopic variation of $v_s$ in the channel due to the nonlocal contributions, which were neglected in our approximation. The error can be estimated from the relation

$$\overline{dv_s/dr} = -\kappa n \ . \tag{39}$$

The value of about 0.002 vortices per $\mu$m$^2$ [Fig. 8(b)] corresponds to a difference in superfluid velocity between the wall and the center of a few mm/s, which is much smaller than the average applied velocity of 118 mm/s. So the influence of the orientation of the vortex tangle on the relative velocities of the two helium components is negligible in this case. However, in general the contribution to the superfluid velocity due to the orientation of the tangle should be taken into account. The same holds for the influence of the mutual friction force density on the normal velocity profile. These effects can become important at higher velocities and may eventually lead to an instability, which can be the origin of the second critical velocity.

## VI. CONCLUSION

We have developed a stable and efficient numerical algorithm and investigated numerically the flow properties of He II in terms of the reconnecting vortex model. In square and circular flow channels a well-defined critical velocity is found. The profile of the normal component velocity has a minor effect on the value of the critical velocity, but it affects the value of the mutual friction force density significantly. The calculated critical velocity agrees with the measured first critical velocity. The calculated mutual-friction force density for a parabolic profile seems to agree with the $T$ I state; the flat profile satisfies more the values found in the $T$ II state.

*Note added in proof.* In addition to what was discussed in Sec. III C with respect to the long term behavior in slits, further calculations have shown that a critical velocity also exists in slits. The main difference with flow channels with square or circular cross sections is that in slits, for velocities below the critical velocity, the vortex tangle evolves into a steady state with (nearly) straight vortex lines while in the other geometries the vortices disappear. Above the critical velocity, in the slit, a vortex tangle remains with fluctuating density which is similar to the other cases. The results for the 50-$\mu$m-wide slit can be summarized in terms of the critical velocity $V_c$

and the parameters $\gamma_L$, $v_{L0}$ introduced in Eq. (31). For flat normal-flow profiles $V_c = 53$ mm/s, $\gamma_L = 1.4 \pm 0.2$ s/mm$^2$, and $v_{L0} = 8 \pm 9$ mm/s. For Poiseuille normal-flow profiles $V_c = 57$ mm/s, $\gamma_L = 0.59 \pm 0.04$ s/mm$^2$, and $v_{L0} = -37 \pm 10$ mm/s.

## ACKNOWLEDGMENTS

We like to thank Arthur Peeters for valuable contributions. H. M. Gijsman is acknowledged for his stimulating interest in our work. We had stimulating and clarifying discussions with K. W. Schwarz, J. T. Tough, H. van Beelen, and J. A. Geurst. This work was partly supported by the Dutch Foundation for the Fundamental Research on Matter (FOM), which is financially supported by the Dutch Organization for the Advancement of Research (NWO). This work was also sponsored by the "Stichting Nationale Computerfaciliteiten" (National Computing Facilities Foundation, NCF) for the use of supercomputerfacilities, with financial support from the Dutch Organization for the Advancement of Research (NWO). The investigations reported in the *note added in proof* were performed by H. R. Penz.

[1] J. T. Tough, in *Progress in Low Temperature Physics,* edited by D. F. Brewer (North-Holland, Amsterdam, 1982), Vol. 8, p. 133.
[2] R. J. Donnelly, *Quantized Vortices in Helium II, Vol. 3 of Cambridge Studies in Low Temperature Physics* (Cambridge University Press, Cambridge, 1991).
[3] K. W. Schwarz, Phys. Rev. Lett. **50**, 364 (1983).
[4] K. W. Schwarz, Phys. Rev. B **31**, 5782 (1985).
[5] K. W. Schwarz, Phys. Rev. B **38**, 2398 (1988).
[6] K. W. Schwarz, Phys. Rev. Lett. **64**, 1130 (1990).
[7] K. W. Schwarz, Phys. Rev. Lett. **69**, 3342 (1992).
[8] C. F. Barenghi, R. J. Donnelly, and W. F. Vinen, J. Low Temp. Phys. **52**, 189 (1983).
[9] J. Crank and P. Nicolson, Proc. Cambridge Philos. Soc. **32**, 50 (1947).
[10] R. G. K. M. Aarts, Ph.D. thesis, Eindhoven, 1993 (unpublished).
[11] A. T. A. M. de Waele and R. G. K. M. Aarts, Phys. Rev. Lett. **72**, 482 (1994).
[12] D. C. Samuels, Phys. Rev. B **46**, 11 714 (1992).
[13] S. S. Courts and J. T. Tough, Phys. Rev. B **39**, 8924 (1989).
[14] G. van der Heijden, A. G. M. van der Boog, and H. C. Kramers, Physica **77**, 487 (1974).
[15] R. R. IJselstein, M. P. de Goeje, and H. M. Kramers, Physica **96B**, 312 (1979).
[16] R. P. Slechtenhorst, G. Marees, and H. van Beelen, Physica **113B**, 341 (1982).
[17] M. P. de Goeje and H. van Beelen, Physica **133B**, 109 (1985).
[18] G. Marees and H. van Beelen, Physica **133B**, 21 (1985).
[19] M. L. Baehr and J. T. Tough, Phys. Rev. B **32**, 5632 (1985).
[20] S. S. Courts and J. T. Tough, Phys. Rev. B **39**, 8942 (1989).
[21] K. P. Martin and J. T. Tough, Phys. Rev. B **27**, 2788 (1983).
[22] D. D. Awschalom, F. P. Milliken, and K. W. Schwarz, Phys. Rev. Lett. **53**, 1372 (1984).
[23] G. Marees, P. J. M. van der Slot, and H. van Beelen, Physica B **114**, 209 (1987).
[24] J. D. Henberger and J. T. Tough, Phys. Rev. B **23**, 413 (1981).
[25] J. G. M. Kuerten, C. A. M. Castelijns, A. T. A. M. de Waele, and H. M. Gijsman, Cryogenics **25**, 419 (1985).
[26] J. C. H. Zeegers, R. G. K. M. Aarts, A. T. A. M. de Waele, and H. M. Gijsman, Phys. Rev. B **45**, 12 442 (1992).
[27] T. Satoh and M. Okuyama, Physica B **165&166**, 759 (1990).
[28] W. F. Vinen, Proc. R. Soc. London, Ser. A **243**, 400 (1957).
[29] W. M. van Alphen, R. de Bruyn Ouboter, K. W. Taconis, and W. de Haas, Physica **40**, 469 (1969).
[30] D. R. Ladner and J. T. Tough, Phys. Rev. B **17**, 1455 (1978).
[31] D. R. Ladner and J. T. Tough, Phys. Rev. B **20**, 2690 (1979).
[32] D. F. Brewer and D. O. Edwards, Philos. Mag. **7**, 721 (1962).
[33] R. K. Childers and J. T. Tough, Phys. Rev. B **13**, 1040 (1976).
[34] C. E. Swanson and R. J. Donnelly, J. Low Temp. Phys. **61**, 363 (1985).
[35] S. S. Courts and J. T. Tough, Phys. Rev. B **38**, 74 (1988).